

Disconnected Lithium Metal Damages Solid-State Electrolytes

Diana Avadanii,^{*,†} Steffen Ganschow,[‡] Markus Stypa,[‡] Sonja Müller,[†] Sabrina Lang,[†] Dominik Kramer,[†] Christoph Kirchlechner,[†] and Reiner Mönig^{*,†}

[†]*Institute for Applied Materials IAM, Karlsruhe Institute of Technology KIT, Karlsruhe, Germany*

[‡]*Leibniz-Institut für Kristallzüchtung IKZ, Berlin, Germany*

E-mail: diana.avadanii@kit.edu; reiner.moenig@kit.edu

Abstract

Solid-state batteries with a lithium-metal anode are energy-storage devices that promise increased energy density and improved safety compared to liquid systems. Despite significant developments, the chemomechanical degradation of solid-state batteries represents a significant challenge to their widespread adoption. Specifically, Li-filled cracks (called “dendrites”) and electronically isolated Li inclusions (“dead” Li) are key defects resulting from coupled electrochemical-mechanical degradation during cycling. In this study, we use a symmetrical Li|LLZO|Li cell with a single-crystal electrolyte and demonstrate that an electronically isolated Li-metal inclusion exhibits bipolarity under an external electrical field, which leads to further crack expansion. We suggest that this process of “dead” metal activation accelerates chemomechanical degradation in solid-state batteries with alkali anodes.

Energy-storage solutions underpin current strategies for the decarbonization of key industries as a step towards achieving carbon neutrality. Using Li-metal anodes (theoretical specific capacity 3862 mAh g⁻¹) and solid-state electrolytes (e.g., Li₇La₃Zr₂O₁₂) improves

17 the energy density and safety of batteries when compared to Li-ion cells using a liquid
18 electrolyte^{1–5}. Studies investigating the chemomechanical processes leading to degradation
19 and short circuits in solid-state batteries (SSBs) pinpoint the nucleation and propagation of
20 Li-filled cracks (i.e., “dendrites”) as the major challenge in the successful implementation
21 of SSBs^{2–4,6–10}.

22 Li-metal electrodeposition and dissolution can lead to the formation of electronically iso-
23 lated Li metal (i-Li or “dead” Li) in both liquid Li-ion^{11,12} and solid-electrolyte cells^{6,13–16}.
24 In liquid Li-ion cells, the formation of electronically disconnected Li is a primary cause of
25 capacity loss and degradation^{11,17}. In solid-state cells, these i-Li islands could be generated
26 during reversal of Li plating and stripping^{13,14,18}, or during heterogeneous Li plating
27 within the grain-boundary network of the solid-state electrolyte^{19–25}. However, the re-
28 sponse during cycling and the impact of these isolated Li-metal inclusions on SSBs remain
29 undetermined. Furthermore, while in other material systems the impact of an electrical
30 field on an isolated metal inclusion in a solid-state ionic conductor is well documented²⁶,
31 similar observations are lacking for Li metal and Li-ion conducting solids⁶.

32 In this study, we aim to directly observe a Li-metal inclusion that is electronically
33 isolated and ionically connected (i-Li) in $\text{Li}_7\text{La}_3\text{Zr}_2\text{O}_{12}$ (LLZO) under an external electrical
34 field. For this purpose we assemble symmetrical $\text{Li}|\text{LLZO}|\text{Li}$ cells with a single-crystal
35 electrolyte and demonstrate that 1) the i-Li metal within the solid electrolyte responds to
36 an applied electrical field (i.e., field-driven migration), 2) mass redistribution of a polarised
37 i-Li in a crack network generates further crack expansion, and 3) redeposition of metal Li
38 in a depleted crack starts at the tip.

39 Our results have wide-ranging implications for solid-state batteries with Li-metal an-
40 odes and, to the best of our knowledge, demonstrate for the first time the field-driven
41 migration of Li metal inside a solid electrolyte and the severe consequences for the me-
42 chanical integrity of the electrolyte^{6,11}.

43 The initiation and propagation of cracks filled with Li metal (“dendrites”) in solid-state

44 electrolytes are influenced by factors such as externally applied load^{10,13}, porosity and
 45 grain size^{27,28}, applied current density¹³, temperature²⁹, dopant content^{9,28}, and asperities
 46 at the Li-metal electrolyte interface^{27,30}. To remove some of these complexities, we use a
 47 fully optically transparent single-crystal LLZO in a symmetrical Li|LLZO|Li cell under
 48 galvanostatic conditions and constant uniaxial load, ranging between 0.23–0.45 $\frac{\text{mA}}{\text{cm}^2}$ and
 49 2–4 MPa, respectively, for each experimental step (Figure 1, Table S1). We use LLZO due to
 50 its interface stability against Li metal, and thus, exclude the formation of an interphase^{5,6}.
 51 We engineer an electronically isolated Li-metal inclusion (i-Li) by growing a dendrite
 52 similar to Figure 1a, and subsequently use the same electrolyte sample reassembled with
 53 electrodes rotated by 90° in a new cell, similar to Figure 1b (Table S1).

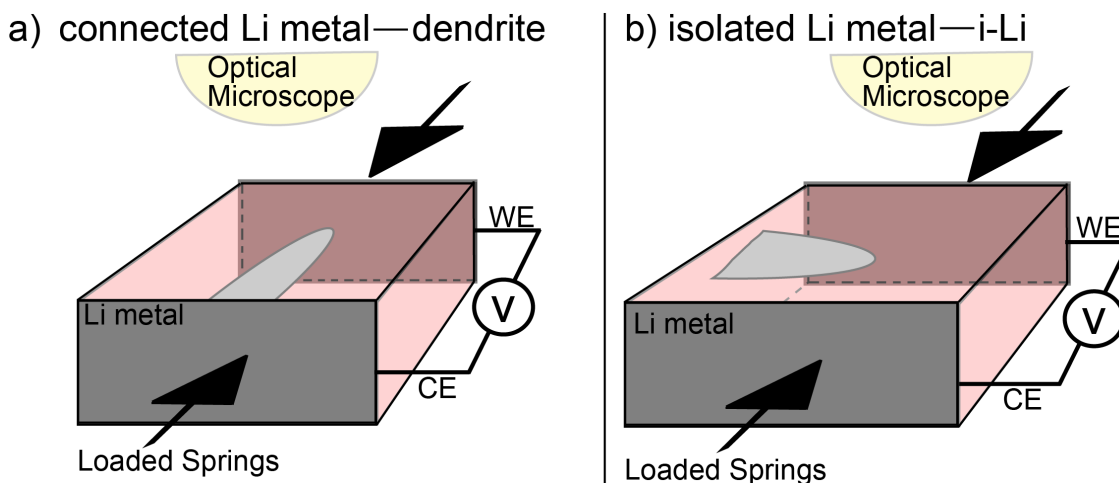


Figure 1: Schematic depicting the experimental setup used in this study. a) Part one of this study reports results in a symmetrical Li|single-crystal LLZO|Li cell under an uniaxial load and constant current. b) Part 2 of this study reports results in a symmetrical cell using the electrolyte from Part 1 reassembled with the electrodes rotated by 90°. This strategy generates a Li-filled crack that is electronically isolated and ionically connected (i-Li).

54 Li dendrite propagation in a single-crystal LLZO

55 Figures 2 and S1 present *operando* observations of a dendrite growing in a single crystal at
 56 an applied nominal current density of $j_n = 0.47 \frac{\text{mA}}{\text{cm}^2}$ and an uniaxial load of 4 MPa (setup
 57 in Figure 1a, Table S1). The dendrites in Figure 2 have a planar, leaf-like morphology and

58 propagate at a rate of $8.6 \frac{\mu\text{m}}{\text{s}}$ (right dendrite) and $4.5 \frac{\mu\text{m}}{\text{s}}$ (left dendrite), respectively. Upon
59 cell disassembly and electrode clean-up, we observe that the two dendrites are connected
60 at the base (Figures S3a, S6c). Our observations of dendrite morphology (Figures S3 and
61 S6) resemble those of Yildirim et al.⁸ and Reisecker et al.³¹ in a similar single-crystal LLZO.
62 We suggest that in a single-crystal LLZO the dendrites propagate as almost-2D objects
63 (thickness $< 2 \mu\text{m}$, Figure S4) on the cleavage plane of the crystal.

64 After dendrite initiation, the local current density increases significantly compared to
65 the nominally applied current density. The observed growth rate of the dendrites, $\frac{dx}{dt}$, in
66 Figures 2 and S1 is enabled by a Li^+ flux concentration at the crack tip under a current
67 density j_{tip} . We write the current, I , as $I = \frac{zFdV}{V_m^{\text{Li}}dt}$, where $z = +1$ for Li, $F = 96485.3 \frac{\text{C}}{\text{mol}}$
68 is the Faraday constant, dV is the change in plated volume, and $V_m^{\text{Li}} = 13.148 \frac{\text{cm}^3}{\text{mol}}$ is the
69 molar volume of Li. Thus, the current density at the tip of the dendrite, j_{tip} , is expressed as

$$j_{\text{tip}} = \frac{I}{A} = \frac{zFAdx}{V_m^{\text{Li}}dt} \frac{1}{A} = \frac{zF}{V_m^{\text{Li}}} \frac{dx}{dt}, \quad (1)$$

70 where the area at the tip of the dendrite, A , cancels out³¹. Note that Equation 1
71 directly relates the observed growth rate with the current density at the crack tip, j_{tip} ,
72 independent of the nominally applied current density, j_n , or the number of simultaneously
73 growing dendrites (Figures 2, S1). The growth rates observed in the experiment in Figure
74 2 correspond to values of $j_{\text{tip}} = 6.3 \frac{\text{A}}{\text{cm}^2}$ for the faster growing dendrite on the right of the
75 image, and $j_{\text{tip}} = 3.3 \frac{\text{A}}{\text{cm}^2}$ for the dendrite on the left. These values are approximately four
76 orders of magnitude larger compared to the nominal current density $j_n = 0.47 \frac{\text{mA}}{\text{cm}^2}$, and
77 highlight the strong localization enabled by Li-metal electrodeposition inside a narrow
78 crack.

79 Our symmetrical cell setup has by design a near-zero open-circuit potential. Thus,
80 the measured cell voltage, under galvanostatic conditions represents the combined input
81 of 1) ohmic resistance of the electrolyte (increases cell voltage, Figures 2), 2) dendrite
82 nucleation at the plating electrode, followed by 3) dendrite propagation and decrease in

effective electrode spacing (decreases cell voltage), and 4) pore formation at the stripping electrode (increases cell voltage). Although we cannot deconvolute the contribution of the aforementioned processes, we suggest that the actual required overpotential for dendrite growth (item 3 above), ΔE_d , is a small fraction of the observed cell voltage in Figures 2 and S1. The maximum stress due to electrodeposition, $\sigma_{0,\max}$, scales with the overpotential according to $\sigma_{0,\max} \approx -\frac{F}{V_m^{\text{Li}}} \Delta E_d$ ²⁷. This stress $\sigma_{0,\max}$ is larger compared to the stress required for crack propagation, σ , approximated as $\sigma \approx \frac{K_{\text{IC}}}{\sqrt{\pi a}}$, where a is the size of the initial surface flaw, and K_{IC} is the fracture toughness of LLZO ($K_{\text{IC}} = 0.6 \text{ MPa}\sqrt{\text{m}}$, measured on a similar single crystal by Swamy et al.³²)²⁷. Thus, electrodeposition in defects on the length scale of $a = 1\text{--}10 \mu\text{m}$ on the Li|LLZO interface (see Figures S1, S4, S6), generates the required stresses for crack propagation ($\sigma \approx 0.33\text{--}0.1 \text{ GPa}$) at relatively small overpotentials, $\Delta E_d \approx 40\text{--}13 \text{ mV}$ ²⁷.

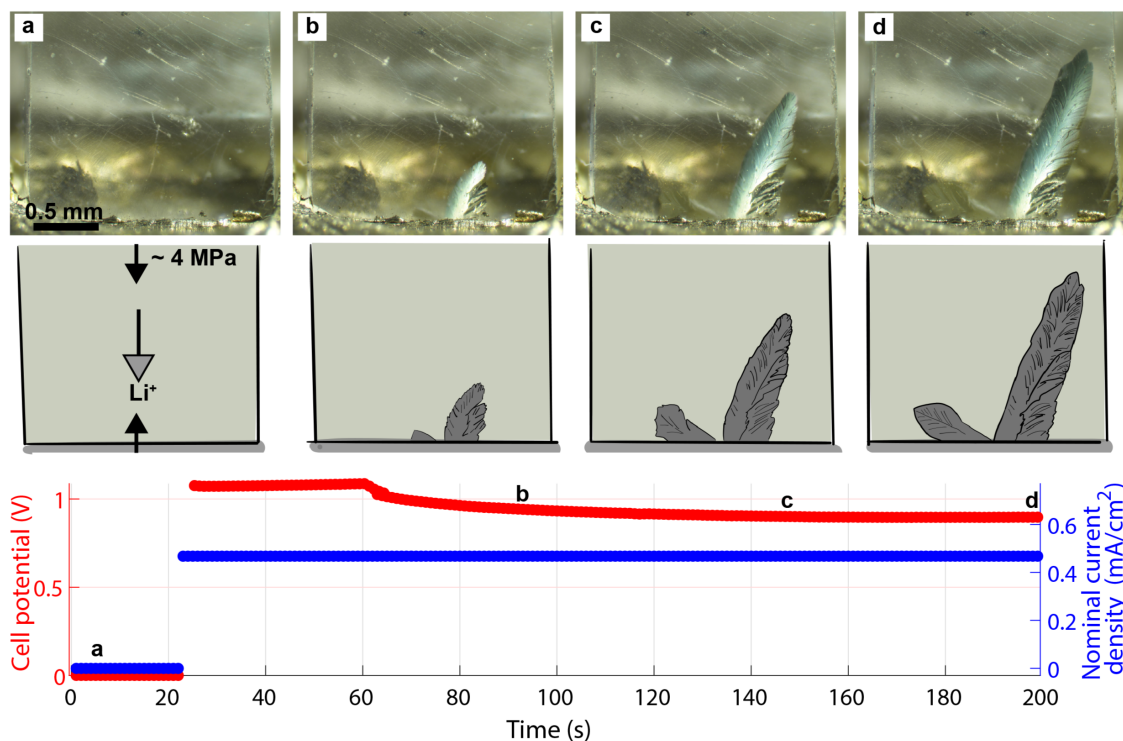


Figure 2: Key frames and corresponding illustrations of dendrite growth in a single-crystal LLZO in the experimental configuration presented in Figure 1a (details in Table S1).

95 **The impact of an electrical field on a Li-metal inclusion in LLZO**

96 Our results demonstrate the field-driven migration of a Li-metal inclusion, which becomes
97 a bipolar electrode²⁶ in LLZO under an electrical field. This phenomenon has been
98 documented in a silver (Ag) particle on the surface of a silver bromide (AgBr) crystal²⁶,
99 and within a Li-metal island in a liquid electrolyte¹¹. Figure 3 summarizes the impact
100 of an electrical field on i-Li, using the setup presented in Figure 1b (see Figure S1 for the
101 initial dendrite propagation). The isolated Li metal displays a shift in mass within the two
102 interconnected cracks, which leads to further crack expansion in Figure 3b (the lower crack
103 grows) and in Figure 3c (the upper crack grows). In Figure 3c Li replates in the upper crack
104 starting at the tip. In later cycles, new dendrites connect the i-Li to the lower electrode
105 (Figure 4). After the reversal of current direction, the Li metal redeposition starts at the
106 tip and edges of the depleted crack network, as displayed in Figure 4 (detailed results
107 using optical microscopy are in Figures S2, S5 and corresponding supplementary videos
108 outlined in Table S1).

109 Figure 5 summarises the mechanisms underpinning our observations (Figures 3, S5).
110 In Figure 5a, the electrical field present within an i-Li inclusion in an LLZO matrix is
111 altered by the redistribution of mobile electrons within the metal. Consequently, the
112 i-Li develops negatively (LLZO|Li(-)) and positively (Li(+)|LLZO) charged regions at
113 the interfaces with the adjacent LLZO^{11,33} (Figure 5a). The presence of the i-Li in the
114 electrolyte enables two Li-ion transport pathways: 1) through the pristine LLZO, and
115 2) through the combined path of the inclusion and the LLZO. Charge transport through
116 the pristine single-crystal LLZO (pathway 1) relies on ion hopping mechanisms and
117 electronic transport between the two electrodes⁵. Transport via the polarized i-Li (pathway
118 2) entails a composite pathway through the solid electrolyte and two charge transfer
119 steps at the inclusion-electrolyte interfaces (Figure 5a). The Li⁺ ions convert into metal
120 at the LLZO|Li(-) interface (deposition), while simultaneously, Li metal dissolution at
121 the Li(+)|LLZO interface enables the charge neutrality of the metal inclusion. These

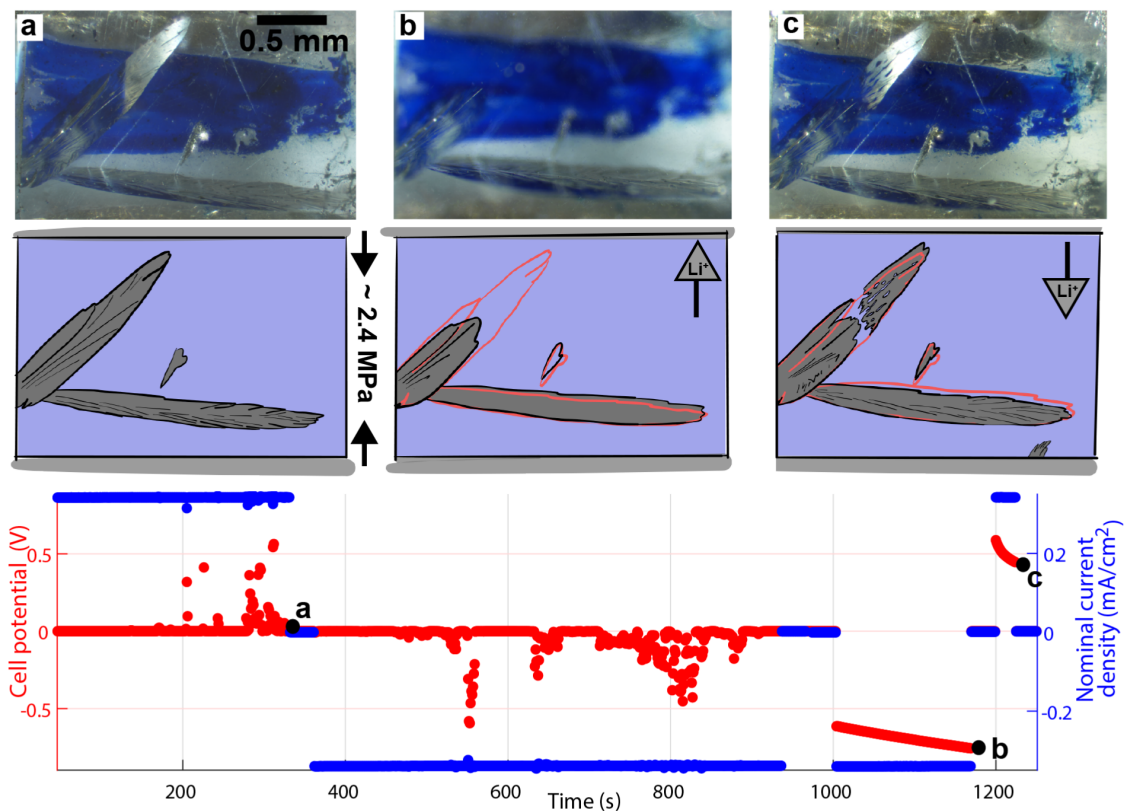


Figure 3: Selected key frames and corresponding schematic displaying evidence of field-driven migration of the bipolar i-Li in LLZO. Note that in subfigure a, the Li-metal within the dendrite mirrors the blue marker dye on the bottom of the crystal. The experimental setup is depicted in Figure 1b. Further details can be found in Figure S2 and Table S1.

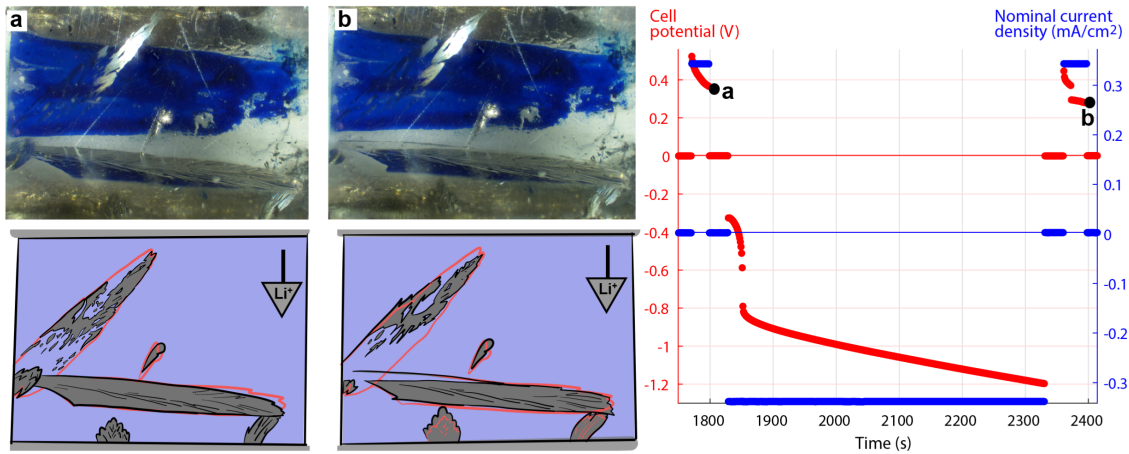


Figure 4: Selected key frames and corresponding schematic displaying evidence of inhomogeneous Li-metal replating in depleted cracks, starting at the tip of the crack. The experimental setup resembles Figure 1b. Further details can be found in Figure S2 and Table S1.

¹²² simultaneous phenomena generate a shift in the centre of mass (i.e., appearance of motion)
¹²³ of the i-Li towards the positive electrode of the cell as displayed in Figure 5b. Unlike a
¹²⁴ liquid Li-ion conductor¹¹, the LLZO does not flow to accommodate the Li deposition at
¹²⁵ the positively polarised end (LLZO|Li(+)) of the inclusion, and the resulting stresses lead
¹²⁶ to crack expansion in the neighbouring LLZO (Figure 5b). Thus, the polarisation of i-Li
¹²⁷ generates further crack propagation while the i-Li mass is conserved (Figures S2, S5).

¹²⁸ The characteristics of a polarised i-Li inclusion impact the Li-ion transfer pathways
¹²⁹ within the cell and consequently, the overall cell impedance³³. The shape, aspect ratio,
¹³⁰ and orientation of the i-Li inclusion with respect to the electrodes affect the electrical field
¹³¹ inside the cell, and therefore, impact the relative contribution of each transport pathway
¹³² and the impedance of the cell. For a bipolar metal, there is no energy threshold for the
¹³³ i-Li mass shift. In the case of an infinitesimally small i-Li, the inclusion carries only small
¹³⁴ currents compared to the bulk electrolyte, which by definition requires that one Li atom is
¹³⁵ deposited and one is dissolved at the inclusion-electrolyte interface. The scaling between
¹³⁶ the i-Li length and the overpotential at the inclusion-electrolyte interface is documented
¹³⁷ in liquid cells by Liu et al.¹¹. Thus, while all i-Li inclusions become polarised, certain
¹³⁸ geometries (e.g., penny shaped and oriented parallel to the electric field) can be particularly
¹³⁹ detrimental for the mechanical integrity of SBBs.

¹⁴⁰ We observe Li re-plating into previously Li-filled cracks that are both electronically
¹⁴¹ isolated (depleted i-Li regions, Figure 3c), and directly connected to one of the electrodes
¹⁴² (depleted dendrites, Figures 4b and S5g). In our optical microscopy observations, the
¹⁴³ re-plating starts in patches at the crack tip or edges, where the distance from the positive
¹⁴⁴ electrode is minimal, and the replated Li metal has an inhomogeneous morphology (Fig-
¹⁴⁵ ures 4 and S5). This observation requires the existence of an electronic conductive pathway
¹⁴⁶ towards an apparently empty crack tip (Figure 5c). We suggest three possible, mutually
¹⁴⁷ compatible, transport paths through: 1) a residual, optically undetectable, Li-metal layer
¹⁴⁸ due to incomplete dissolution, 2) the LLZO fracture surface due the local changes in

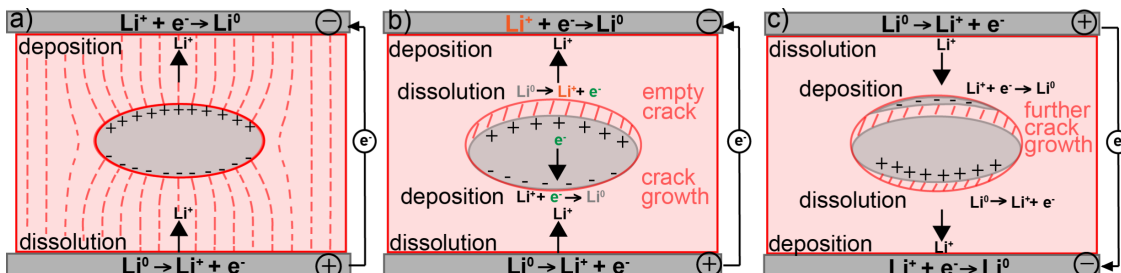


Figure 5: a) Illustration of an electronically isolated (i-Li) inclusion in a solid electrolyte that becomes bipolar under an external electrical field. The presence of i-Li alters the field lines and enables two transport pathways. b) The resulting charge separation due to polarisation leads to simultaneous dissolution and deposition at the particle interfaces, generating the appearance of motion towards the positive electrode and an empty crack towards the negative electrode. c) The reversal of the polarity of the external field leads to inhomogeneous re-deposition towards the positive electrode. The black arrows correspond to the direction of the current in the LLZO and the metal inclusion.

149 stoichiometry, and 3) the instantaneous deposition of trace amounts of Li metal on the
 150 crack surface generated during current reversal. The first transport path is the least likely,
 151 as it implies that the electrochemical force driving Li dissolution does not overcome the
 152 adhesion between the thin Li and LLZO, which has been documented as an interface
 153 with weak adhesion due to the relatively poor Li wetting of surfaces^{34–36}. The second
 154 possible electron transport path relies on the local changes in the electronic conductivity of
 155 the LLZO fractured surface (i.e., the density of states around the Fermi level). Moreover,
 156 local heterogeneities on the fracture surface of the LLZO can lead to increases in the local
 157 conductivity. The third possible electron transport path relies on the fast redeposition of an
 158 optically undetectable, Li-metal layer on the crack surface, which enables the preferential
 159 Li redeposition such that electrode distance is reduced (i.e., at the crack tip). The Li patches
 160 we observe during redeposition in Figures 4 and S5 could be a consequence of Li dewetting
 161 at high homologous temperatures (0.66 for Li at room temperature) in order to minimise
 162 surface energy³⁷. Each patch polarises as an individual i-Li, and thus, contributes to the
 163 inhomogeneous lithium morphology at the crack tip. Morphological instability during the
 164 deposition of isolated metal towards the positive electrode has also been observed on the
 165 surface of AgBr²⁶. Furthermore, our observations highlight that the rate of redeposition in

¹⁶⁶ a Li-metal depleted crack is faster compared to simultaneous crack opening and Li-metal
¹⁶⁷ plating during dendrite growth (Figure 2).

¹⁶⁸ Implications for solid-state batteries

¹⁶⁹ Our results have direct implications for all SSBs with metal anodes, which could contain
¹⁷⁰ metallic inclusions in the electrolyte due to heterogeneous plating and stripping, or cell
¹⁷¹ assembly. Solid-state cells rely on ceramic electrolytes manufactured through various
¹⁷² techniques (e.g., tape casting^{38,39}, pulsed laser deposition⁴⁰, powder aerosol deposition⁴¹)
¹⁷³ leading to large variability in porosity, electrolyte thickness, and grain-size distribution.
¹⁷⁴ This microstructural heterogeneity can lead to asymmetric Li plating and stripping and
¹⁷⁵ eventual “dead” Li formation^{13–15}. Within the same electrolyte sample, differences in grain-
¹⁷⁶ boundary electrical and mechanical properties enable heterogeneous ionic and electronic
¹⁷⁷ conductivities leading to Li-metal deposition in subsurface voids^{25,42} and at susceptible
¹⁷⁸ grain boundaries^{19,21,43}, which can become subsequently polarised and accelerate elec-
¹⁷⁹ trolyte damage. Particles of i-Li can also form as a consequence of battery architecture,
¹⁸⁰ such as engineered 3D electrolytes acting as a porous frame for Li plating³⁹ or multilayered
¹⁸¹ structures⁴⁴. Thus, cycling SSBs with i-Li generates further crack opening or new cracks
¹⁸² with each cycle and accelerates mechanical damage.

¹⁸³ In summary, we have demonstrated that Li-metal inclusions in a solid-state electrolyte
¹⁸⁴ exhibit bipolarity and field-driven migration. Our strategy of removing and rotating the
¹⁸⁵ electrodes in a symmetrical cell with a single-crystal electrolyte after dendrite growth
¹⁸⁶ creates an electronically isolated and ionically connected inclusion (i-Li). The current
¹⁸⁷ through the cell generates an electrical field around the i-Li (leading to polarisation), which
¹⁸⁸ provides the driving force for further crack expansion due to simultaneous deposition and
¹⁸⁹ dissolution of Li metal under high hydrostatic stresses within the crack. We expect this
¹⁹⁰ mechanism to operate in solid-state batteries with alkali metal anodes that have “dead”

¹⁹¹ metal inclusions, and suggest that the polarization of these particles in SSBs is particularly
¹⁹² destructive due to their ability to accelerate mechanical damage within the cell.

193 **Acknowledgement**

194 The authors thank Mr Edmund Böck for technical support in manufacturing the optical
195 cell setup. DA thanks Dr Xufei Fang for stimulating conversations.

196 **Supporting Information Available**

197 Extended experimental methods, details of galvanostatic experiments, and *operando* re-
198 sults.

199 **References**

- 200 (1) Albertus, P.; Anandan, V.; Ban, C.; Balsara, N.; Belharouak, I.; Buettner-Garrett, J.;
201 Chen, Z.; Daniel, C.; Doeuff, M.; Dudney, N. J.; others Challenges for and pathways
202 toward Li-metal-based all-solid-state batteries. 2021.
- 203 (2) Schmaltz, T.; Hartmann, F.; Wicke, T.; Weymann, L.; Neef, C.; Janek, J. A Roadmap for
204 Solid-State Batteries. *Advanced Energy Materials* **2023**, *13*, 2301886.
- 205 (3) Kazyak, E.; García-Méndez, R. Recent progress and challenges for manufacturing and
206 operating solid-state batteries for electric vehicles. *MRS Bulletin* **2024**, 1–13.
- 207 (4) Janek, J.; Zeier, W. G. Challenges in speeding up solid-state battery development.
208 *Nature Energy* **2023**, *8*, 230–240.
- 209 (5) Samson, A. J.; Hofstetter, K.; Bag, S.; Thangadurai, V. A bird's-eye view of Li-stuffed
210 garnet-type Li₇La₃Zr₂O₁₂ ceramic electrolytes for advanced all-solid-state Li
211 batteries. *Energy & Environmental Science* **2019**, *12*, 2957–2975.
- 212 (6) Krauskopf, T.; Richter, F. H.; Zeier, W. G.; Janek, J. Physicochemical concepts of the
213 lithium metal anode in solid-state batteries. *Chemical reviews* **2020**, *120*, 7745–7794.

- 214 (7) Ning, Z.; Li, G.; Melvin, D. L.; Chen, Y.; Bu, J.; Spencer-Jolly, D.; Liu, J.; Hu, B.; Gao, X.;
215 Perera, J.; others Dendrite initiation and propagation in lithium metal solid-state
216 batteries. *Nature* **2023**, *618*, 287–293.
- 217 (8) Yildirim, C.; Flatscher, F.; Ganschow, S.; Lassnig, A.; Gammer, C.; Todt, J.; Keckes, J.;
218 Rettenwander, D. Understanding the origin of lithium dendrite branching in Li₆.
219 5La₃Zr_{1.5}Ta_{0.5}O₁₂ solid-state electrolyte via microscopy measurements. *Nature
220 Communications* **2024**, *15*, 8207.
- 221 (9) Flatscher, F.; Todt, J.; Burghammer, M.; Søreide, H.-S.; Porz, L.; Li, Y.; Wenner, S.;
222 Bobal, V.; Ganschow, S.; Sartory, B.; others Deflecting dendrites by introducing com-
223 pressive stress in Li₇La₃Zr₂O₁₂ using ion implantation. *Small* **2024**, *20*, 2307515.
- 224 (10) Fincher, C. D.; Athanasiou, C. E.; Gilgenbach, C.; Wang, M.; Sheldon, B. W.;
225 Carter, W. C.; Chiang, Y.-M. Controlling dendrite propagation in solid-state batteries
226 with engineered stress. *Joule* **2022**, *6*, 2794–2809.
- 227 (11) Liu, F.; Xu, R.; Wu, Y.; Boyle, D. T.; Yang, A.; Xu, J.; Zhu, Y.; Ye, Y.; Yu, Z.; Zhang, Z.;
228 others Dynamic spatial progression of isolated lithium during battery operations.
229 *Nature* **2021**, *600*, 659–663.
- 230 (12) Chen, X.-R.; Yan, C.; Ding, J.-F.; Peng, H.-J.; Zhang, Q. New insights into “dead
231 lithium” during stripping in lithium metal batteries. *Journal of Energy Chemistry* **2021**,
232 *62*, 289–294.
- 233 (13) Kazyak, E.; Garcia-Mendez, R.; LePage, W. S.; Sharifi, A.; Davis, A. L.; Sanchez, A. J.;
234 Chen, K.-H.; Haslam, C.; Sakamoto, J.; Dasgupta, N. P. Li penetration in ceramic
235 solid electrolytes: operando microscopy analysis of morphology, propagation, and
236 reversibility. *Matter* **2020**, *2*, 1025–1048.
- 237 (14) Sun, H.; Liu, Q.; Chen, J.; Li, Y.; Ye, H.; Zhao, J.; Geng, L.; Dai, Q.; Yang, T.; Li, H.; others

- 238 In situ visualization of lithium penetration through solid electrolyte and dead lithium
239 dynamics in solid-state lithium metal batteries. *ACS nano* **2021**, *15*, 19070–19079.
- 240 (15) Hu, X.; Zhang, Z.; Zhang, X.; Wang, Y.; Yang, X.; Wang, X.; Fayena-Greenstein, M.;
241 Yehezkel, H. A.; Langford, S.; Zhou, D.; others External-pressure–electrochemistry
242 coupling in solid-state lithium metal batteries. *Nature Reviews Materials* **2024**, *9*, 305–
243 320.
- 244 (16) Cao, T.; Xu, R.; Cheng, X.; Wang, M.; Sun, T.; Lu, J.; Liu, X.; Zhang, Y.; Zhang, Z.
245 Chemomechanical Origins of the Dynamic Evolution of Isolated Li Filaments in
246 Inorganic Solid-State Electrolytes. *Nano Letters* **2024**, *24*, 1843–1850.
- 247 (17) Fang, C.; Li, J.; Zhang, M.; Zhang, Y.; Yang, F.; Lee, J. Z.; Lee, M.-H.; Alvarado, J.;
248 Schroeder, M. A.; Yang, Y.; others Quantifying inactive lithium in lithium metal
249 batteries. *Nature* **2019**, *572*, 511–515.
- 250 (18) Guo, W.; Shen, F.; Liu, J.; Zhang, Q.; Guo, H.; Yin, Y.; Gao, J.; Sun, Z.; Han, X.; Hu, Y.
251 In-situ optical observation of Li growth in garnet-type solid state electrolyte. *Energy
Storage Materials* **2021**, *41*, 791–797.
- 252 (19) Song, Y.; Yang, L.; Zhao, W.; Wang, Z.; Zhao, Y.; Wang, Z.; Zhao, Q.; Liu, H.; Pan, F.
253 Revealing the short-circuiting mechanism of garnet-based solid-state electrolyte.
254 *Advanced Energy Materials* **2019**, *9*, 1900671.
- 255 (20) Han, F.; Westover, A. S.; Yue, J.; Fan, X.; Wang, F.; Chi, M.; Leonard, D. N.; Dud-
256 ney, N. J.; Wang, H.; Wang, C. High electronic conductivity as the origin of lithium
257 dendrite formation within solid electrolytes. *Nature Energy* **2019**, *4*, 187–196.
- 258 (21) Aguesse, F.; Manalastas, W.; Buannic, L.; Lopez del Amo, J. M.; Singh, G.; Llordés, A.;
259 Kilner, J. Investigating the dendritic growth during full cell cycling of garnet elec-
260 trolyte in direct contact with Li metal. *ACS applied materials & interfaces* **2017**, *9*,
261 3808–3816.

- 263 (22) Sun, M.; Liu, T.; Yuan, Y.; Ling, M.; Xu, N.; Liu, Y.; Yan, L.; Li, H.; Liu, C.; Lu, Y.; others
264 Visualizing lithium dendrite formation within solid-state electrolytes. *ACS Energy*
265 *Letters* **2021**, *6*, 451–458.
- 266 (23) Tian, H.-K.; Liu, Z.; Ji, Y.; Chen, L.-Q.; Qi, Y. Interfacial electronic properties dictate Li
267 dendrite growth in solid electrolytes. *Chemistry of Materials* **2019**, *31*, 7351–7359.
- 268 (24) Tian, H.-K.; Xu, B.; Qi, Y. Computational study of lithium nucleation tendency in
269 Li₇La₃Zr₂O₁₂ (LLZO) and rational design of interlayer materials to prevent lithium
270 dendrites. *Journal of Power Sources* **2018**, *392*, 79–86.
- 271 (25) Zhao, J.; Tang, Y.; Dai, Q.; Du, C.; Zhang, Y.; Xue, D.; Chen, T.; Chen, J.; Wang, B.;
272 Yao, J.; others In situ observation of Li deposition-induced cracking in garnet solid
273 electrolytes. *Energy & Environmental Materials* **2022**, *5*, 524–532.
- 274 (26) Peppler, K.; Reitz, C.; Janek, J. Field-driven migration of bipolar metal particles on
275 solid electrolytes. *Applied Physics Letters* **2008**, *93*.
- 276 (27) Porz, L.; Swamy, T.; Sheldon, B. W.; Rettenwander, D.; Frömling, T.; Thaman, H. L.;
277 Berendts, S.; Uecker, R.; Carter, W. C.; Chiang, Y.-M. Mechanism of lithium metal
278 penetration through inorganic solid electrolytes. *Advanced Energy Materials* **2017**, *7*,
279 1701003.
- 280 (28) Huang, X.; Lu, Y.; Guo, H.; Song, Z.; Xiu, T.; Badding, M. E.; Wen, Z. None-mother-
281 powder method to prepare dense Li-garnet solid electrolytes with high critical current
282 density. *ACS Applied Energy Materials* **2018**, *1*, 5355–5365.
- 283 (29) Wang, M.; Wolfenstine, J. B.; Sakamoto, J. Temperature dependent flux balance of the
284 Li/Li₇La₃Zr₂O₁₂ interface. *Electrochimica Acta* **2019**, *296*, 842–847.
- 285 (30) Lee, K.; Sakamoto, J. Li Stripping Behavior of Anode-Free Solid-State Batteries Un-

- 286 der Intermittent-Current Discharge Conditions. *Advanced Energy Materials* **2024**, *14*,
287 2303571.
- 288 (31) Reisecker, V.; Flatscher, F.; Porz, L.; Fincher, C.; Todt, J.; Hanghofer, I.; Hennige, V.;
289 Linares-Moreau, M.; Falcaro, P.; Ganschow, S.; others Effect of pulse-current-based
290 protocols on the lithium dendrite formation and evolution in all-solid-state batteries.
291 *Nature Communications* **2023**, *14*, 2432.
- 292 (32) Swamy, T.; Park, R.; Sheldon, B. W.; Rettenwander, D.; Porz, L.; Berendts, S.; Uecker, R.;
293 Carter, W. C.; Chiang, Y.-M. Lithium metal penetration induced by electrodeposition
294 through solid electrolytes: example in single-crystal $\text{Li}_6\text{La}_3\text{ZrTaO}_{12}$ garnet. *Journal of The
295 Electrochemical Society* **2018**, *165*, A3648–A3655.
- 296 (33) Squires, T. M.; Bazant, M. Z. Induced-charge electro-osmosis. *Journal of Fluid Mechanics*
297 **2004**, *509*, 217–252.
- 298 (34) Wang, J.; Wang, H.; Xie, J.; Yang, A.; Pei, A.; Wu, C.-L.; Shi, F.; Liu, Y.; Lin, D.; Gong, Y.;
299 others Fundamental study on the wetting property of liquid lithium. *Energy Storage
300 Materials* **2018**, *14*, 345–350.
- 301 (35) Wang, M.; Sakamoto, J. Correlating the interface resistance and surface adhesion of
302 the Li metal-solid electrolyte interface. *Journal of Power Sources* **2018**, *377*, 7–11.
- 303 (36) Han, X.; Gong, Y.; Fu, K.; He, X.; Hitz, G. T.; Dai, J.; Pearse, A.; Liu, B.; Wang, H.;
304 Rubloff, G.; others Negating interfacial impedance in garnet-based solid-state Li metal
305 batteries. *Nature materials* **2017**, *16*, 572–579.
- 306 (37) Thompson, C. V. Solid-State Dewetting of Thin Films. *Annual Review of Materials
307 Research* **2012**, *42*, 399–434.
- 308 (38) Fu, Z.; Zhang, L.; Gritton, J. E.; Godbey, G.; Hamann, T.; Gong, Y.; McOwen, D.;
309 Wachsman, E. Probing the mechanical properties of a doped $\text{Li}_7\text{La}_3\text{Zr}_2\text{O}_{12}$ garnet

- 310 thin electrolyte for solid-state batteries. *ACS applied materials & interfaces* **2020**, *12*,
311 24693–24700.
- 312 (39) Yang, C.; Zhang, L.; Liu, B.; Xu, S.; Hamann, T.; McOwen, D.; Dai, J.; Luo, W.; Gong, Y.;
313 Wachsman, E. D.; others Continuous plating/stripping behavior of solid-state lithium
314 metal anode in a 3D ion-conductive framework. *Proceedings of the National Academy of
315 Sciences* **2018**, *115*, 3770–3775.
- 316 (40) Pfenninger, R.; Struzik, M.; Garbayo, I.; Stilp, E.; Rupp, J. L. A low ride on processing
317 temperature for fast lithium conduction in garnet solid-state battery films. *Nature
318 Energy* **2019**, *4*, 475–483.
- 319 (41) Nazarenus, T.; Sun, Y.; Exner, J.; Kita, J.; Moos, R. Powder Aerosol Deposition as a
320 Method to Produce Garnet-Type Solid Ceramic Electrolytes: A Study on Electrochem-
321 ical Film Properties and Industrial Applications. *Energy Technology* **2021**, *9*, 2100211.
- 322 (42) Shen, F.; Dixit, M. B.; Xiao, X.; Hatzell, K. B. Effect of pore connectivity on Li dendrite
323 propagation within LLZO electrolytes observed with synchrotron X-ray tomography.
324 *ACS Energy Letters* **2018**, *3*, 1056–1061.
- 325 (43) Raj, R.; Wolfenstine, J. Current limit diagrams for dendrite formation in solid-state
326 electrolytes for Li-ion batteries. *Journal of Power Sources* **2017**, *343*, 119–126.
- 327 (44) Doerrer, C.; Metzler, M.; Matthews, G.; Bu, J.; Spencer-Jolly, D.; Bruce, P. G.; Pasta, M.;
328 Grant, P. S. Spraying Li₆PS₅Cl and silver-carbon multilayers to facilitate large-scale
329 fabrication of all-solid-state batteries. *Device* **2024**, *2*.

TOC Graphic

331

